LANGMUIR

Generality of Evaporative Crystal Liftoff on Heated Hydrophobic Substrates

Pranjal Agrawal, Virkeshwar Kumar, Samantha McBride, and Susmita Dash*

Cite This: *Langmuir* 2023, 39, 7578−7589

Read Online

ACCESS | Metrics & More | Article Recommendations | Supporting Information

ABSTRACT: Scaling or mineral fouling occurs due to the presence of dissolved minerals in water. Scaling is problematic in numerous industrial and household plumbing applications where water is used. The current methods of scale removal often utilize harsh chemicals that are not environmentally friendly. The evaporation of a saline droplet provides a platform to study the role of the substrate in the dynamics of crystallization during scaling. In the present work, we show out-of-plane growth of crystal deposits during the evaporation of saline droplets of aqueous potassium chloride on a heated smooth and microtextured hydrophobic substrate. These out-of-plane deposits, termed as "crystal legs", are in minimal contact with the substrate and can be easily removed from the substrate. The out-of-plane evaporative crystallization of saline droplets of different initial volumes and concentrations is observed irrespective of the chemistry of the hydrophobic coating and the crystal habits investigated. We attribute this general behavior of crystal legs to the growth and stacking of smaller crystals (size $\sim 10~\mu m$) between the primary crystals toward the end of evaporation. We show that the rate at which the crystal legs grow increases with an increase in the substrate temperature. A mass conservation model is applied to predict the leg growth rate, which agrees well with the experiments.

$C_{initial} = 0.5 C_{sat}$ $C_{initial} = C_{sat}$
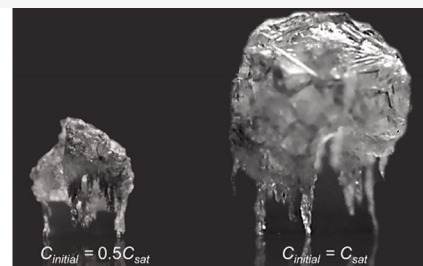
Evaporative crystal liftoff on a heated hydrophobic substrate

■ INTRODUCTION

Mineral fouling, also called scaling, occurs in numerous industries including thermal powerplants,[1−4] desalination plants,[5,6] evaporative depositions on ship hulls,[7] and household applications such as reverse osmosis system membranes.[8] Inorganic fouling creates resistance to thermal and fluid transport, resulting in reduced system efficiency.[9,10] The scaling on heat exchangers is primarily caused by salts such as calcium sulfate and calcium carbonate with negative solubility with temperature, while the scaling during desalination and deposition on ship hulls are also attributed to salts such as sodium chloride and potassium chloride that have positive solubility with temperature.[4,7] Mechanical and chemical methods typically used to remove the scale deposits result in significant downtime of equipment, high maintenance costs, and negative environmental impacts.[11] It is therefore important to devise methods for mitigation and easy removal of inorganic fouling. The evaporation of a saline sessile droplet depends on the water activity coefficient, relative humidity, substrate properties, and temperature.[4,12−16] The evaporation of a saline droplet on a heated substrate offers a simple platform to understand crystallization-induced scale formation and their remedies by taking into account the influence of salts and the underlying substrate on crystallization.

During evaporation of a saline droplet, crystallization occurs at a critical supersaturation depending on the interfacial surface energies.[14,17] The evaporative deposition pattern of saline droplets depends on the initial contact angle and contact angle hysteresis that determine the droplet evaporation mode.[18] The

evaporative deposit morphologies range from coffee-ring deposits on hydrophilic substrates[19] to condensed deposits on hydrophobic and liquid-impregnated surfaces.[20,21] On hydrophilic surfaces, the in-plane orientation of crystal growth along the substrate and pinning of salt crystals at the droplet triple contact line make removal of crystalline deposits difficult.[20] Localized salt deposits on hydrophobic surfaces are relatively easier to remove from the substrate due to lower adhesion between the deposits and the substrate compared to that on hydrophilic substrates.

Varying crystal deposit shapes and characteristics arise from saline drops evaporated on hydrophobic and superhydrophobic surfaces of different coatings and textures.[22,23] Evaporation of droplets of aqueous sodium chloride (NaCl) on a heated hexamethyldisiloxane-coated polypropylene textured superhydrophobic substrate resulted in igloo- and pebble-shaped deposits.[22] Self-lifting salt deposits during evaporation of a saturated sodium chloride solution droplet were observed on a octadecyltrichlorosilane (OTS)-coated smooth hydrophobic substrate at room temperature but not for substrates coated with polydimethylsiloxane (PDMS).[23] The absence of self-

Table 1. Different Salts and Initial Saline Concentrations, Test Substrates, and Temperatures Used in the Experiments

substrates	salts (solubility g/mL)	concentration	substrate temperature
R0PDMS, R0Silane, R0OTS, R0Teflon, R10Silane, R100Silane	KCl (0.35), NaCl (0.36), KNO$_3$(0.31), NH$_4$Cl (0.38)	$0.00625C_{sat} - C_{sat}$ for KCl, C_{sat} for other salts	25, 50, 70, 80, 95 °C

lifting behavior on PDMS was attributed to the lower hydrophobicity of PDMS compared to OTS.[23] On specific nanotextured superhydrophobic surfaces with non-communicating air gaps, crystals of NaCl grown from evaporating drops self-eject from the underlying substrate at elevated temperatures.[24] Long vertical crystalline deposits were reported to form due to the metastable Cassie−Baxter state of the droplet on the substrate with local Wenzel contacts, which led to localized crystallization and eventual lifting of the entire deposit.[24] Vertical growth of crystals was also demonstrated for different salts including NaCl, KCl, NH$_4$Cl, Na$_2$SO$_4$, and CuSO$_4$ on heated superhydrophobic nanotextured substrates while being absent on smooth silanized [trichloro-(1H,1H,2H,2H-perfluorooctyl)silane] hydrophobic substrates.[24] The discrepancy in the nature of evaporative salt deposition on the smooth hydrophobic substrate was attributed to the difference in the initial volume of the droplet and the amount of dissolved salts.[23,24] A saturated saline droplet with a higher initial volume has more crystallizing mass and was reported to cause crystallization along the substrate, thus reducing the extent of out-of-plane growth of crystals.[24]

Crystalline self-ejection has garnered significant attention because of the potential to facilitate self-cleaning of salt deposits from underlying substrates. So far, investigations into this effect have been restricted to the formation of crystal legs on smooth OTS-coated[23] or Teflon-coated substrates[25] and on a specific nanotextured substrate[24] for a given initial volume of a saturated saline droplet. A general mechanism of the self-liftoff of the salt crystals during evaporation of saline droplets, which is independent of the orientation of nucleated crystals[23] and the initial volume of the droplet[24] on different hydrophobic substrates at different temperatures, is lacking.

Here, we systematically investigate the formation of out-of-plane crystal deposits (aka, crystalline self-liftoff) on hydrophobic substrates as a function of (1) the droplet volume, (2) the crystal morphology, and (3) the specific chemistry of the hydrophobic coating. We show that the time instants for crystal nucleation and that for crystal leg growth are dependent on the substrate−air surface energy and the temperature of the substrate. The crystal deposits are composed of primary crystals of size on the order of 100 μm and secondary crystals of size ~10 μm that make up the crystal legs. We propose a mechanism regarding the formation of the crystal legs based on the relative affinity between the saline solution with the salt crystals versus the underlying substrate and propose a model for the leg growth rate based on liquid transport through a porous crystal network and evaporation at different substrate temperatures.

■ MATERIALS AND METHODS

Evaporative deposition of droplets of aqueous solutions of different salts' morphology—sodium chloride (NaCl, cubic), potassium chloride (KCl, cubic), potassium nitrate (KNO$_3$, orthorhombic), and ammonium chloride (NH$_4$Cl, cubic)—on different hydrophobic substrates is investigated. These salts show different crystal habits such as cubic (NaCl and KCl), acicular or needle-like (KNO$_3$), and dendritic (NH$_4$Cl) during evaporative crystallization on heated

hydrophobic surfaces (Supplementary Information).[26] Saline solutions with different initial concentrations (C_{sat}, $0.5C_{sat}$, $0.1C_{sat}$, $0.05C_{sat}$, $0.0125C_{sat}$, and $0.00625C_{sat}$) are prepared using deionized (DI) water and salts (purity > 99.9% from Merck Emparta). In the present study, the saturation concentration (C_{sat}) of the aqueous solution is defined at 25 °C.

Smooth hydrophobic and microtextured superhydrophobic substrates are used here. Four different kinds of hydrophobic coatings— PDMS, trichloro(1H,1H,2H,2H-perfluorooctyl)silane (fluorosilane), Teflon (Dupont AF-2400X), and octadecyltrichlorosilane (OTS)— are used to render smooth glass substrates hydrophobic. The substrates are referred to as RXC, where X is 0 for smooth substrates and represents the spacing between the micropillars for the textured substrates and C represents the hydrophobic coating used on the substrate. The corresponding substrates are referred to as R0PDMS, R0Silane, R0Teflon, and R0OTS. The glass slide is initially cleaned by sequentially ultrasonicating in acetone, isopropyl alcohol (IPA), and DI water. For the PDMS coating, a mixture of silicone elastomer and a curing agent (Dowsil 184 Silicone Elastomer Curing Agent) in a ratio of 10:1, respectively, is spin-coated on a glass substrate (6000 rpm for 1 min) and subsequently baked in an oven at 95 °C for 90 min. For the silane coating, a precleaned glass slide is plasma-cleaned (Plasma Cleaner PDC-002, Harrick Plasma) for 15 min. The plasma-cleaned glass slide is vapor-deposited with fluorosilane for 12 h in a desiccator. The excess silane coating is removed via ultrasonication in acetone and IPA. R0Teflon is prepared by using the 2% wt/vol Teflon solution (prepared by dissolving Teflon particles in FC40) spin-coated on the glass slide at 6000 rpm for 1 min and cured at 90 °C for 10 min. The R0OTS substrate is fabricated by immersing the glass slide into a mixture of 0.33 vol % silane in toluene and sonicating it for 2 min and then adding a 0.65 vol % emulsion of DI water and toluene and sonicating for 2 min. The excess OTS is removed through ultrasonication in acetone and IPA. The contact angles (CAs) of a water droplet (3 μL) on the R0PDMS, R0Silane, R0Teflon, and R0OTS substrates at room temperature are measured using a contact angle meter (Dataphysics OCA 15A) to be 108 ± 3°, 115 ± 2°, 125 ± 3°, and 109 ± 2°, respectively.

The textured superhydrophobic surfaces comprise a silicon pillar array hydrophobized using fluorosilane, which has a thickness of <2 nm.[27] The textured silicon substrate is prepared using a standard photolithography technique to create square pillar arrays of width w = 10 μm, height h = 12 μm, and interpillar spacing d = 10 and 100 μm. The textured substrates are referred to as R10 (d = 10 μm) and R100 (d = 100 μm). The textured silicon substrate is rendered hydrophobic by vapor deposition of fluorosilane (method discussed earlier) and is referred to as R10Silane and R100Silane. The CAs of a water droplet (3 μL) on the R10Silane and R100Silane substrates at room temperature (=25 °C) are measured to be 153 ± 3° and 152 ± 2°.

The side-view evaporation experiments are conducted by gently placing a saline droplet using a micropipette on the test substrates maintained at different temperatures (50, 70, 80, and 95 °C) using a hot plate (Thermo Scientific, Cimarec) with a temperature variation of around ±1 °C (Table 1). In the case of the smooth hydrophobic R0PDMS substrate, additional experiments are conducted by placing the test substrates on a clean indium tin oxide (ITO)-coated glass substrate maintained at specific temperatures by resistive heating using a DC power supply (GW Instek, GPE-2323). For all the experiments, the temperature at the top of the test substrate is measured using a K-type surface thermocouple (Omega) with an accuracy of 0.75% of the measured value and a hand digital temperature logger (Omega). For the experiments on pillared surfaces (R10Silane and R10Silane), the surface thermocouple is attached beside the textured portion of the substrate to measure the

temperature of the substrate. The transparency of ITO glass (90% transmissivity) and PDMS coating gives an opportunity to visualize the crystallization process in the saline droplet from the bottom (Figure 1). Simultaneous side- and bottom-view images of evaporative
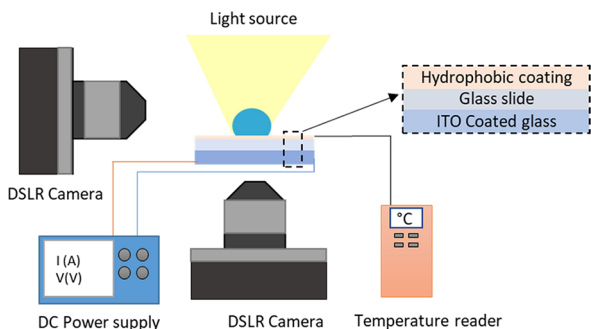

Figure 1. Experimental setup for the side and bottom visualization of salt crystallization during evaporation of a saline droplet on the test substrate heated using an ITO-coated heating surface connected to a DC power supply.

crystallization are obtained using DSLR cameras (Nikon D850 and Nikon Z7-II) coupled with Navitar zoom lenses (Navitar 6× and Navitar coaxial-12×) with front light illumination (Dolan Jenner MI-152). During the experiments, the ambient temperature and relative humidity are maintained at 25 ± 1 °C and 50 ± 5%. Saline droplets of different initial concentrations with initial volumes of 3 μL $(0.00625C_{sat} - C_{sat})$, 5 μL (C_{sat}), or 15 μL (C_{sat}) are gently placed on the test substrate, and evaporation is monitored in terms of the variation in contact radius, height, time instant of nucleation, and crystallization behavior. Experiments for each variable are repeated at least three times.

RESULTS AND DISCUSSION

Effect of Salt Morphology. The experiments are initially performed on a heated R0PDMS substrate $(T = 80 °C)$ with saturated aqueous solutions of different salts (NaCl, KCl, KNO$_3$, and NH$_4$Cl) (Supplementary Video S1). In general, on a hydrophobic surface, droplet evaporation initially occurs in a constant contact radius (CCR) mode and then in a constant contact angle (CCA) mode where the contact diameter reduces along with the reduction in the droplet height (Figure 2a–e).[28,29] The evaporation of droplets of the saturated aqueous solution of all the salts considered in our study on the R0PDMS substrate at $T = 80 °C$ occurs in the CCR mode (details in Supplementary Figure S2). Crystallization initiates near the triple contact line and at the liquid–air interface when the droplet reaches a critical supersaturation that ranges from 1.1 to 1.6 for different salts (Table 2 and Supplementary Videos S2, S3).[30,31] The crystal nucleation is observed to occur at a supersaturation greater than 1 because of the higher free energy barrier for nucleation in the case of hydrophobic substrates.[14] The free energy barrier for heterogeneous nucleation depends on interfacial surface tension between the substrate and the crystal, solution, and air along with the temperature of the substrate,[26,32] $\Delta G'_{crit} = \frac{4\pi V_m^2}{3(k_B T \ln S)^2}\gamma_{CrL}^3(2 + m)(1 - m)^2$, where γ_{CrL} is the interfacial surface tension between the crystal embryo (Cr) and the saline solution (L), $m = \frac{\gamma_{SubL} - \gamma_{CrSub}}{\gamma_{CrL}}$, where γ_{CrSub} is the interfacial surface tension between the crystal (Cr) and the substrate (sub), and γ_{SubL} is the interfacial surface tension between the substrate (Sub) and the solution (L), S is the supersaturation

of the solution, V_m is the molecular volume of the crystal embryo, k_B is the Boltzmann constant, and T is the temperature of the solution.

The nucleated crystals are vertically oriented at the liquid–air interface due to the hydrophobic nature of the substrate.[20] The growth of crystals near the triple contact line leads to outward wicking of the saline solution in the horizontal direction, leading to an increase in the footprint area of the droplet and crystal deposition on the substrate.[33,34] Toward the end of evaporation, the crystals are observed to grow out-of-plane upward at several locations from the base of the droplet (Figure 2a–d). The out-of-plane growth of the crystals, forming a leg-like structure, lifts the accumulated crystal deposit and is observed for all the conditions tested (i.e., all four hydrophobic chemistries and the four salts considered).

Sodium chloride and potassium chloride have cubic crystal habits and similar solubility at room temperature (~0.35 g/mL) but nevertheless exhibit different final leg heights during evaporative crystallization at 80 °C (Figure 2a,b,e,f). Figure 2e,f shows the contact diameter and height of the evaporating droplet till it forms the crystal deposit and shows liftoff during the evaporation of sessile droplets of aqueous KCl and NaCl on the R0PDMS substrate. The contact diameter is measured till distinct crystal legs are observed, and the deposit height is calculated from the base of the deposit to the topmost point of the deposit (inset in Figure 2e). During evaporation of a sessile droplet of aqueous NaCl, the crystal deposit grows in the horizontal and vertical directions to form a cauliflower-like structure[11,27] (Figure 2b,f) (further details in the Supplementary Information). However, in the case of the aqueous KCl droplet, the crystal deposits primarily grow in the vertical direction (Figure 2a,e), resulting in higher heights of the crystal legs compared to that of NaCl (Figure 2c). In the case of KNO$_3$ and NH$_4$Cl salt solutions, the crystals first cover the outer liquid–air surface of the droplet (Figure 2c,d). The presence of the salt shell at the liquid–air interface inhibits the evaporation rate and leads to an increase in time duration before which the growth of the crystal legs is observed. For instance, during evaporation of a 3 μL droplet of saturated KCl and NaCl solutions, the crystal legs are observed at ~47 and ~62 s, respectively, while in the case of NH$_4$Cl and KNO$_3$ solutions, the crystal legs are observed at ~94 and 106 s. In the case of a saline droplet with NH$_4$Cl and KNO$_3$, the formation of the crystal shell inhibits visualization from below. Because KCl exhibited the most dramatic liftoff behavior, we use aqueous KCl for the remainder of the experiments presented here to probe the out-of-plane crystal growth phenomena at different initial concentrations, drop volumes, and on different substrates.

Dynamics of Crystallization. Simultaneous top- and bottom-view imaging is used to visualize evaporative deposition of the droplet of aqueous KCl on the heated R0PDMS substrate $(T = 70 °C$ as the visualization was more clear in this case) to provide a better understanding of the transport behavior at the liquid–solid interface (Figure 3a,b) (also shown in Supplementary Movie S1). During evaporation of the sessile saline droplet, crystals nucleate as the local supersaturation exceeds critical supersaturation, and the corresponding time instant is marked as $t_{nucleation}$ (=35 s in Figure 3a,b). These crystals are termed as "primary crystals". Because of the hydrophobic nature of the substrate, the primary crystals orient vertically and are not pinned to the triple contact line and move freely in the droplet due to
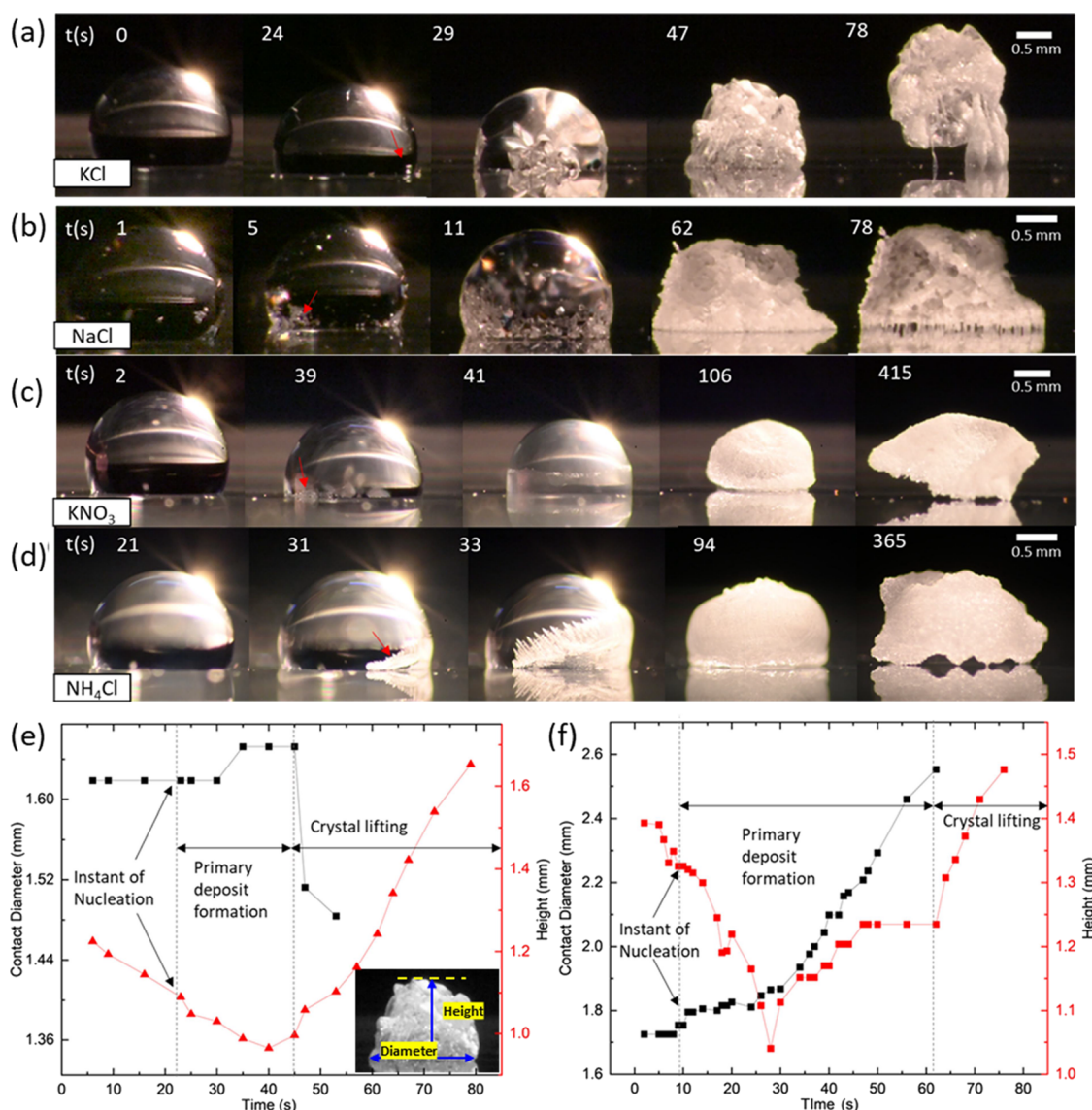
Figure 2. Representative images showing evaporation and out-of-plane crystallization of a 3 μL saline droplet with different salts (a) KCl, (b) NaCl, (c) KNO$_3$, and (d) NH$_4$Cl on a heated PDMS substrate ($T = 80$ °C). The contact diameter (black square) and height (red triangle) of an evaporating droplet of aqueous saturated (e) KCl and (f) NaCl on the R0PDMS substrate at $T = 80$ °C corresponding to the experimental dataset shown in Figure 2a,b, respectively. The inset in Figure 2e shows the contact diameter and height of the KCl crystal deposit.

Table 2. Supersaturation and Nucleation Time Instant for a Droplet (Initial Volume of 3 μL) of Saturated Aqueous Solutions of Various Salts (KCl, NaCl, KNO$_3$, and NH$_4$Cl) Averaged over Three Experimental Datasets on the R0PDMS Substrate at $T = 80$ °C

salt	supersaturation	nucleation time (s)
KCl	1.4 ± 0.1	27 ± 4
NaCl	1.1 ± 0.06	10 ± 1
NH$_4$Cl	1.55 ± 0.05	30 ± 11
KNO$_3$	1.5 ± 0.07	35 ± 5

buoyancy and Marangoni convection.[35,36] These primary crystals agglomerate and eventually settle on the substrate due to the volumetric growth ($t = 57$ s, Figure 3a,b) and form a crystal network while the droplet evaporates.[14,37−39] Once the crystals settle down and the crystal form a network, further movement of the liquid in the primary crystal network is not expected to be influenced by the internal convective flows

inside the droplet. The time duration over which the primary crystal deposit forms and the arrangement of the crystals on the substrate depend on the surface energy of the hydrophobic coating.[40,41] The liquid dewets from the hydrophobic surface while remaining pinned to the hydrophilic crystals ($t = 70$ s marked as dashed lines in Figure 3b) due to the lower contact line pinning of the liquid on the hydrophobic surface.[42,43] During dewetting, the thin liquid film between the primary crystals and the substrate forms capillary liquid bridges (marked by yellow dashed lines at $t = 87$ s in Figure 3a). Volumetric losses from the liquid bridge due to evaporation are compensated by continuous wicking of the liquid between the primary crystals from the top of the deposit toward the substrate (Figure 3d). Due to the high evaporation rate in the thin capillary liquid bridges, small crystals[44] with a size (<10 μm) significantly smaller than the size of primary crystals (~100 μm) are formed (Figure 3c,d). These smaller crystals are termed as "secondary crystals". The continuous stacking up of the secondary crystals between the primary crystals and the
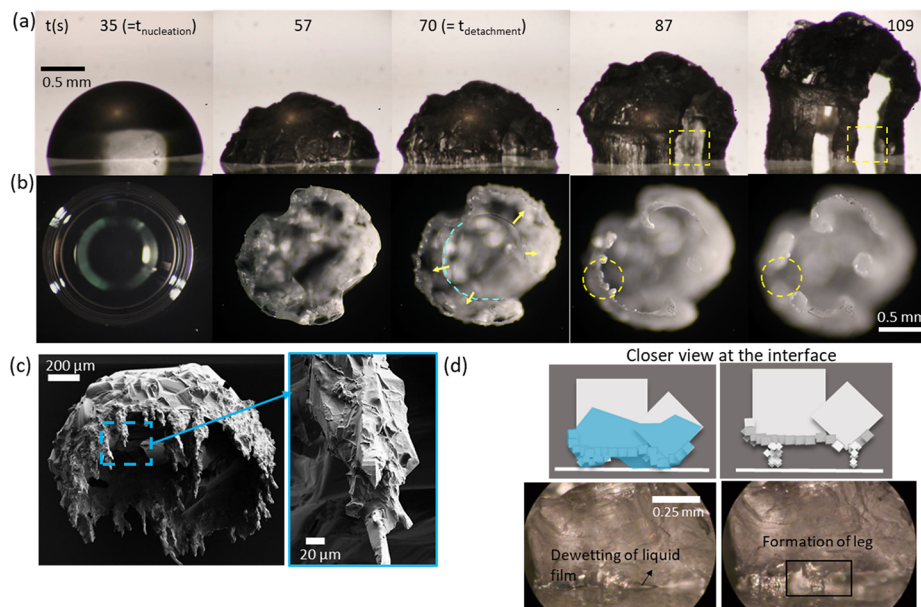
Figure 3. Simultaneous (a) side and (b) bottom visualization of the evaporation of a saturated aqueous KCl droplet on the R0PDMS surface at $T =$ 70 °C. Nucleation of crystals near the contact line is observed at $t = 35$ s; $t = 57$ s marks the formation of the primary crystal deposit. In (b), the dashed light blue curve and the yellow arrows at $t = 70$ s show the dewetting of the liquid from the substrate. The marked circular region (yellow dashed) in the bottom view and the square marked region in the side-view image at $t = 87$ and $t = 109$ s show the rupturing or merging of the capillary liquid bridge. (c) Scanning electron microscopy (SEM) image of the crystalline deposit comprised primary crystals and secondary crystals forming the crystal legs (inset, marked in blue dashed line). (d) Close-up view at the crystal–liquid–substrate interface showing dewetting of the thin liquid film and formation of the crystalline leg.

substrate leads to the formation of crystal legs and vertical lifting of the entire crystal network (Figure 3d). The capillary liquid bridges detach from the substrate as the deposit lifts after which we observe the final crystal legs (as can be observed in the dashed square in the last two panels in Figure 3a,b). The time instant when the lifting of the primary crystal deposit starts is marked as $t_{\text{detachment}}$ (=70 s in Figure 3a,b). Toward the end of evaporation, the average size of secondary crystals reduces due to the low availability of the solution[24] and the legs taper off (Figure 3c inset). These pointed legs are minimally and weakly attached to the hydrophobic substrate and can be removed easily.

The formation of the crystal legs depends on the dewetting of the liquid from the substrate and the wicking of the dewetted solution into the porous crystal networks. The absence of a primary crystal network during saline droplet evaporation of low-solubility salts (i.e., calcium sulfate, 0.003 g/mL) or a dilute salt solution (0.1 M or 0.005 g/mL) of sodium chloride on hydrophobic substrates is one reason why crystal legs have not been observed for those compositions[14,20,30,45] (details are included in the Supplementary Information, Figure S4). The formation of a primary crystal deposit is necessary to form crystal legs as it enables the liquid to dewet from the hydrophobic substrate to the hydrophilic crystals. We expect a similar mechanism for the formation of crystal legs in the evaporative deposition of droplets of aqueous NaCl, KNO_3, and NH_4Cl solutions. The bottom-view visualization of crystallization and the liquid dewetting at the base of the droplets of saturated KNO_3 and NH_4Cl solutions is challenging because of the presence of the salt crystal shell, while dewetting similar to that in the KCl solution droplet is observed in the bottom-view visualization of a droplet of saturated aqueous NaCl (Supplementary Information).

Effect of Surface Coatings and Roughness. The surface energy of the substrate is a combination of polar and dispersive energy components ($\gamma_{sa} = \gamma_{sa}^{polar} + \gamma_{sa}^{dispersive}$). Low surface energy coatings like fluorosilane, PDMS, and Teflon inhibit crystal nucleation on the substrate due to the low ratio of the polar to dispersive surface energy components, $\gamma_{sa}^{polar}/\gamma_{sa}^{dispersive} < 0.1$.[40] The crystals grown on these materials do not pin to the substrate, and we observe formation of crystal legs and crystal liftoff on all the test substrates investigated (R0PDMS, R0OTS, R0Silane, R0Teflon, and R100Silane) except for R10Silane (Figures 2a, 4a–c, and 5a,b). The surface energy of the substrate influences the time instant of initiation of the crystal leg ($t_{\text{detachment}}$ at $h_{\text{leg}} = 0$ in Figure 4d) when the primary crystal starts lifting from the substrate. For the smooth substrates at 80 °C, crystal legs form at an earlier time ($t_{\text{detachment}} = 48$ and 49 s) on R0PDMS and R0OTS compared
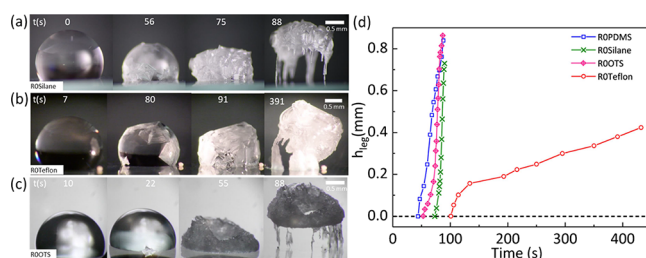

Figure 4. Representative images showing evaporative crystallization in a saturated saline droplet (3 μL, KCl) on (a) R0Silane, (b) R0Teflon, and (c) R0OTS substrates maintained at $T = 80$ °C; the scale bar represents 0.5 mm. (d) Growth of the crystal legs toward the end of evaporation on different substrates at $T = 80$ °C corresponding to the experimental dataset shown in Figure 4a–c; time corresponding to $h_{\text{leg}} = 0$ marks the time instant corresponding to detachment ($t_{\text{detachment}}$) of the crystal deposit.
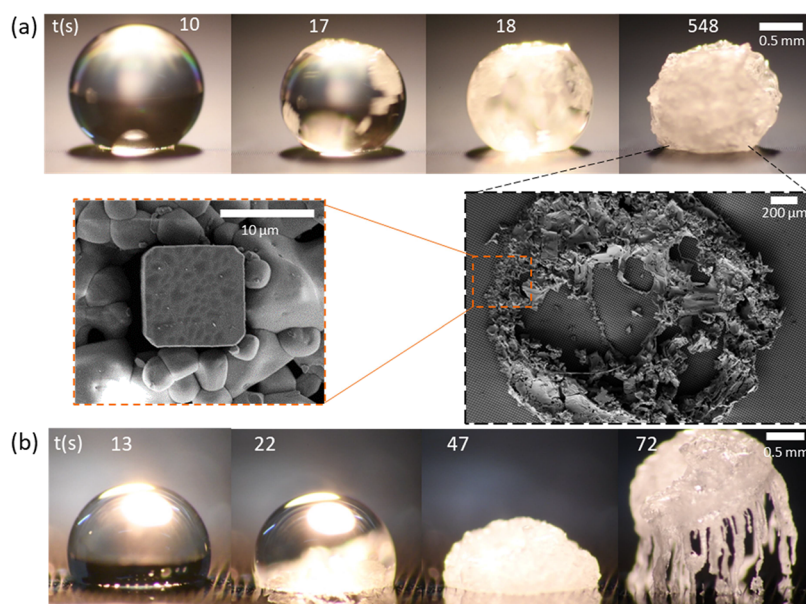
Figure 5. (a) Evaporation of a droplet of aqueous KCl (initial volume = 3 μL) on the R10Silane substrate at $T = 80$ °C; the SEM images are taken after removing the top portion of the deposit and show the secondary salt crystals formed in the space between the pillars; the zoomed inset of the SEM image shows the crystallization around a single micropillar. (b) Side-view images of evaporative crystallization of a droplet of aqueous KCl on the R100Silane substrate maintained at $T = 80$ °C.

Table 3. Measured Values of CA of the Droplet on Different Substrates at Room Temperature and CA, Supersaturation, Instant of Nucleation, and Detachment of Crystals at 80 °C[a]

substrate	θ_c (room temperature)	θ_c (heated surface)	supersaturation	nucleation time $t_{nucleation}$ (s)	detachment time, $t_{detachment}$ (s)
R0PDMS	108 ± 3°	107 ± 3°	1.31 ± 0.03	22 ± 1	48 ± 8
R0Silane	115 ± 2°	115 ± 3°	1.51 ± 0.17	33 ± 3	79 ± 9
R0Teflon	125 ± 3°	125 ± 3°	1.42 ± 0.1	49 ± 5	91 ± 4
R0OTS	109 ± 2°	107 ± 2°	1.3 ± 0.06	22 ± 2	49 ± 2
R10Silane	155 ± 3°	140 ± 7°	1.3 ± 0.15	22 ± 6	
R100Silane	154 ± 2°	117 ± 2°	1.28 ± 0.08	16 ± 1	46 ± 2

[a]The data is averaged over three experimental datasets.

to R0Silane ($t_{detachment}$ = 79 s) and R0Teflon ($t_{detachment}$ = 91 s) (Figure 2a,4a−c and Table 1).[15,16,32] The difference in the time of detachment of the primary crystals from the various hydrophobic substrates can be attributed to the difference in the nucleation time of the crystals. The nucleation of crystals occurs when the saline droplet evaporates on the hydrophobic surface and reaches an average supersaturation of approximately 1.31 ± 0.03, 1.3 ± 0.05, 1.42 ± 0.11, and 1.51 ± 0.17 on R0PDMS, R0OTS, R0Teflon, and R0Silane, respectively, which is attributed to the difference in the surface energy of the coatings and the CA of the droplet on the substrate (Table 3).[40,46] The variability in the time instant of detachment of the crystal deposit from the substrate is due to its dependence on the time instant of nucleation and the agglomeration of the crystals to form a crystal network. The experimentally measured crystal leg radius and the crystal leg growth rate are calculated when distinct crystal legs are observed after the detachment of the crystal deposit in the experiments. The radius of the crystal legs and the rate of growth of crystal legs are observed to be dependent on the underlying substrates (Figure 4d). For instance, at $T = 80$ °C, the crystal leg has a radius of ~10 μm and a growth rate of ~40 μm/s on R0Silane, while the crystal leg radius and the growth rate on R0Teflon are ~100 μm and ~5 μm/s, respectively (details in the Supplementary Information). For a given initial volume of the

saline droplet (3 μL), using the vapor-diffusion model, the evaporation flux is inversely related to the droplet CA (Supplementary Section S6).[47,48] At higher CAs, evaporative flux is lower (see Supplementary Figure S6), so the time required for a droplet to reach critical supersaturation is also higher. The lower rate of evaporation on R0Teflon (CA ~ 125°) compared to that on R0PDMS (CA ~ 108°) and R0OTS (CA ~ 107°) in conjunction with higher supersaturation for salt nucleation results in a higher $t_{nucleation}$ ~ 49 s on R0Teflon compared to R0PDMS and R0OTS that exhibit $t_{nucleation}$ ~ 22 s on both the substrates. Subsequently, $t_{detachment}$ on R0Teflon, R0PDMS, and R0OTS is 91, 48, and 49 s, respectively (Table 1). Similarly, $t_{nucleation}$ on R0Silane (CA −115°) is ~33 s, and $t_{detachment}$ is ~79 s, which lies between the $t_{detachment}$ on R0PDMS, R0OTS, and R0Teflon.

The introduction of microtextures on a hydrophobic substrate renders it superhydrophobic with the droplet sitting on top of the pillared structures [also known as the Cassie−Baxter (CB) state]. Substrate heating alters substrate wettability as well as the droplet wetting state, which can induce a transition from the CB to the Wenzel state.[49] The CA of a 3 μL droplet on the textured substrates maintained at $T = 80$ °C is measured to be lower than that at room temperature (Table 3). The CA of the saline droplet on heated R10Silane is measured to be ~140° (Figure 5a), which is closer to its CB
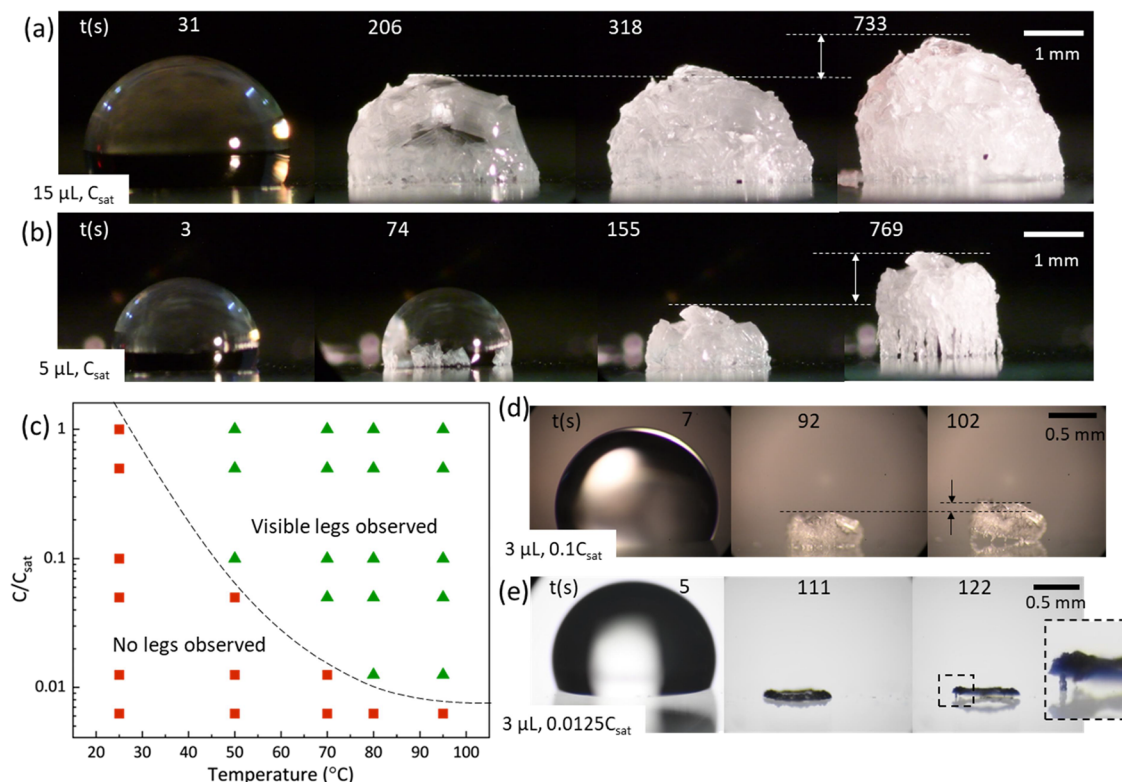
Figure 6. Evaporation of droplets of saturated aqueous KCl with initial volume (V_i) equal to (a) 15 μL and (b) 5 μL. (c) Phase diagram for the formation of visible crystal legs during evaporation of droplets of saturated aqueous KCl with $V_i = 3$ μL and varying the solute concentrations on the R0PDMS substrate at various temperatures. Evaporation of a droplet ($V_i = 3$ μL) with initial concentrations equal to (d) $0.1C_{sat}$ and (e) $0.0125C_{sat}$ on R0PDMS at $T = 80$ °C. The dashed lines in (a), (b), and (d) indicate the vertical growth of the legs.

CA ($\theta^c = \cos^{-1}(\varphi_s(1 + \cos\theta_Y) - 1) = 148°$, where φ_s is the solid fraction of the pillared surface $= w^2/(d + w)^2$) and θ_Y is Young's CA of the droplet on a smooth substrate.[50,51] The CA of the droplet on heated R100Silane (CA ~ 117°) (Figure 5b) is closer to the Wenzel CA ($\theta^w = \cos^{-1}(r_w \cos\theta_Y) = 115.7°$, where $r_w = 1 + 4wh/(d + w)^2 = 1.04$ is the Wenzel roughness factor (actual area/projected area), suggesting that the droplet is in the Wenzel state. The pinning force on the droplet increases when the droplet transitions from the CB state to the Wenzel state. The pinning force (F_p) on the droplet per unit contact line length (l) can be defined as $F_p/l = r_w\gamma_{la} \sin\theta^{rec}$, where θ^{rec} is the receding CA of the liquid droplet on the plain substrate of similar chemistry and γ_{la} is the surface tension at the liquid−air interface.[51] The Wenzel roughness factor (r_w) for R10Silane is 2.2, while that of the R100Silane substrate is 1.04, which is comparable to the roughness factor of a smooth substrate ($r = 1$).

Despite having similar surface chemistry, crystal legs are observed on R100Silane and not on R10Silane (Supplementary Video S4). This behavior can be attributed to the difference in wetting transitions on the two substrates due to the onset of crystallization (Figure 5a,b). In the case of the R10Silane substrate, the droplet is initially in the CB state which has multiple nucleation sites due to the presence of air pockets in the microtextures.[26] The crystals nucleate near the edge of the pillars (at the solid−liquid−vapor interface) and provide a path for the liquid to creep inside the microtextures causing the transition from the CB to the Wenzel state, which increases the contact diameter of the deposit (details in the Supplementary Information).[24] These crystals (size < 10 μm) get pinned between the microtextures ($d = 10$ μm) and

continue to grow between the pillars (shown in the inset of Figure 5a). The pinning force in these crystals is high compared to crystals that grow on an R100Silane substrate due to the higher roughness factor and thus leg formation is inhibited. The superhydrophobic substrate used by Shin et al.[22] comprises textures of size ~5−10 μm, and the crystals are pinned in between the textures, which explains the absence of crystal leg formation. Crystal leg formation on the specific nanotextured surface occurs due to non-communicating pore structures where the droplet is in the metastable Cassie and Wenzel state, leading to preferential leg formation from the Wenzel contacts.[24]

Effect of the Droplet Initial Volume and Concentration. The height of the crystal legs depends on the stacking of the secondary crystals formed after the liquid in the droplet dewets from the substrate and wicks inside the primary crystals. Thus, the final height of the crystal legs is limited by the amount of the saline solution present in the primary crystal deposit, and out-of-plane growth continues until complete evaporation of the liquid. At a particular temperature, the final crystal leg height depends on a number of parameters related to the crystal formation, growth, and arrangement of crystals on the substrate, which is a stochastic process.[14,26,29,45] Experiments with saturated saline droplets with different initial volumes (V_i) are conducted to investigate the effect of crystallizing mass on the formation of crystal legs. During evaporative crystallization in a saturated saline droplet of higher initial volumes (15 and 5 μL) on the R0PDMS substrate at $T = 80$ °C, the number of crystal legs increases, and the legs are not distinct (Figure 6a,b). These deposits are cleaned easily from the substrate, which suggests that even
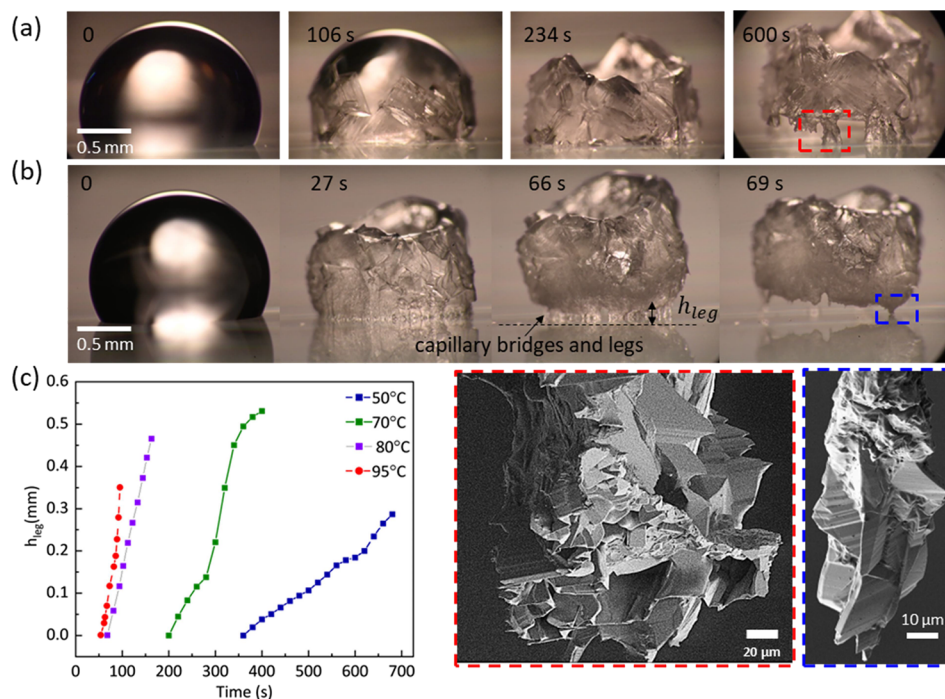
Figure 7. Effect of temperature on the evaporation of a 3 μL droplet of aqueous KCl on the PDMS substrate at (a) 50 °C and (b) 95 °C; the marked areas (red and blue dashed lines) in the insets show the SEM images of the legs formed from stacking of secondary crystals. At 95 °C, the formation and rupture of capillary bridges can be observed at $t \sim 66$ s. (c) Representative experimental datasets showing the temporal variation of the crystal leg height on the R0PDMS substrate at different temperatures.

though legs are not distinct, the contact area of the deposit on the substrate is limited. Distinct leg formation is visible at a lower volume (3 μL) of saturated saline droplets on R0PDMS at $T = 80$ °C (Figure 2a).

The effect of low crystallizing mass is explored in a saline droplet with $V_i = 3$ μL on the R0PDMS substrate. The amount of crystallizing mass is varied by reducing the concentration of the solute in the aqueous solution. The formation of distinct crystal legs at different initial concentrations (C) is dependent on the temperature of the substrate, which can be observed from the phase diagram plotted for $V_i = 3$ μL on the R0PDMS substrate (Figure 6c). For instance, at $T = 80$ °C, distinct crystal legs are observed at concentrations C_{sat}, $0.5C_{sat}$, $0.1C_{sat}$, $0.05C_{sat}$, and $0.0125C_{sat}$ (Figure 6d,e), while no legs are observed when the concentration is reduced to $0.00625C_{sat}$. At lower salt concentrations ($0.0125C_{sat}$) (Figure 6e), the droplet volume reaches as low as 1.6−2% of their initial volume ($V_i = 3$ μL), which is around 50 nL, before crystal nucleation is observed. The lower initial concentration of the saline solution results in a lower amount of the liquid present in the primary crystal deposit, which leads to a reduction in the crystal leg height. For instance, at $T = 80$ °C, the crystal leg height observed in the case of a 3 μL droplet of saturated aqueous KCl is 1.1−3 times the height observed when the concentration was reduced to $0.5C_{sat}$ and $0.1C_{sat}$ (Figures 2a, 6d). For $0.0125C_{sat}$, a ring-shaped crystal network is formed, and crystal legs are observed toward the end of evaporation (inset of Figure 6e). This suggests that the mechanism of the formation of legs on smooth substrates is only due to the formation of a crystal network and can be observed even when the initial volume of the droplet is low (50 nL), unlike that reported earlier.[24] At the lowest concentration ($0.00625C_{sat}$), crystal deposition shows a ring-shaped crystal network without the formation of crystal legs even at a substrate temperature of

95 °C (details in the Supplementary Information, Figure S4c). Interestingly, a higher droplet volume ($V_i = 6$ μL) with the initial concentration ~$0.00625C_{sat}$ at 95 °C shows the formation of crystal legs (details in the Supplementary Information, Figure S4d). This suggests that a minimum amount of salt is required for visible crystal leg formation at each temperature. For instance, at 80 °C, the minimum amount of salt in the aqueous solution that shows visible leg formation is ~0.00125 g. It is worth noting that the aqueous solution of calcium sulfate (CaSO$_4$) does not exhibit crystal legs even when the initial volume of the droplet is 400 μL, i.e., ~0.0013 g dissolved salt (details in the Supplementary Information).

Effect of the Substrate Temperature. The effect of the substrate temperature on the formation of the crystal legs during evaporation of a 3 μL droplet with a saturation concentration is investigated on the R0PDMS substrate maintained at 50, 70, and 95 °C (Figure 7a,b) At room temperature, the distinct crystal legs are not visible on R0PDMS; however, we do observe the formation of secondary crystals (details in Supplementary Figure S8), and the final deposit can be easily removed without leaving any crystal residue on the substrate. Due to the lower evaporation rate at room temperature, there is a preference for crystal growth over nucleation of new crystals,[17,52] which leads to a larger size and a lower number of primary crystals. As a result, there is also a reduction in the formation and stacking of secondary crystals in the vertical direction. At room temperature, evaporative flux remains almost constant for different CAs greater than 90° (Supplementary Information), and thus, dewetting of the liquid from the crystals is a function of crystal arrangement on the surface. Heating increases the evaporation flux on the droplet and reduces the $t_{detachment}$ causing earlier dewetting of the liquid compared to room temperature and thus forms
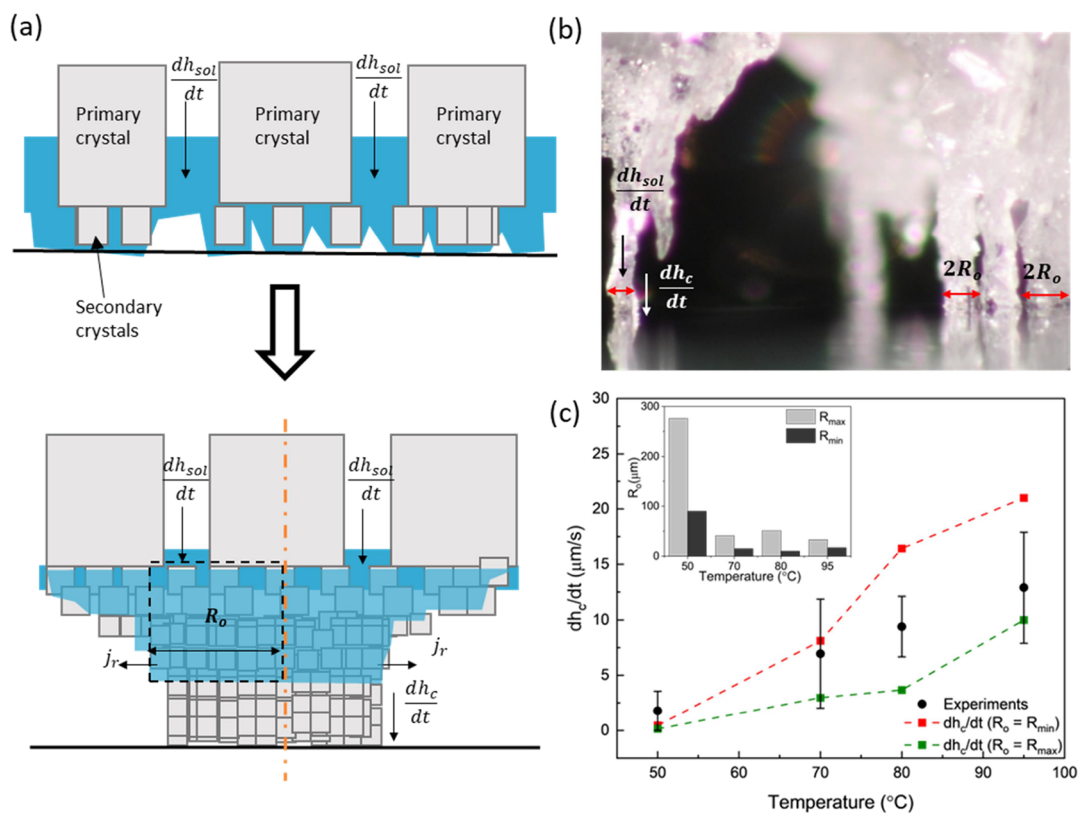
Figure 8. (a) Schematic of the saline solution present between the initial primary crystals and the secondary crystals; the wicking of liquid in the crystals and its evaporation lead to the stacking of secondary crystals forming crystal legs. The black dashed square represents the 1D control volume for evaporation of the liquid. (b) Experimental image of crystal legs on a heated R0PDMS substrate at $T = 70$ °C, with red arrows pointing to varying leg diameter ($= 2R_o$), black arrows to the wicking speed (dh_{sol}/dt), and white arrows to the growth of crystal legs (dh_c/dt). (c) Experimental and predicted crystal growth rate (dh_c/dt) at different substrate temperatures; the inset shows the maximum and minimum crystal leg radius observed at different temperatures.

secondary crystals and crystal legs. The time instants $t_{nucleation}$ and $t_{detachment}$ are lower at a higher substrate temperature due to the high evaporation rate. For instance, at 95 °C, $t_{nucleation} \sim$ 18 s and $t_{detachment} \sim 65$ s compared to $t_{nucleation} \sim 97$ s and $t_{detachment} \sim 300$ s at 50 °C (Figure 7a,b).

The substrate temperature influences the size of primary (Figure 7a,b) and secondary crystals and the average diameter of the crystal legs (inset, Figure 7a,b). The crystal legs initiate in the gaps between two adjacent primary crystals. With an increased substrate temperature, the number of crystals nucleating increases, which leads to the formation of smaller crystals.[26] The smaller gap between the primary crystals at a higher temperature leads to formation of thinner capillary bridges, which either rupture or merge to form thinner crystal legs (at $t = 66$ s, Figure 7b). For example, the average leg thickness reduces from 180 ± 93 μm at 50 °C to 50 ± 16 μm at 95 °C (details in the Supplementary Information, Figure S9). Deviations in the crystal leg radius are due to the stochastic nature of crystal nucleation, which influences the final height and diameter of the crystal legs. However, the average rate of growth of the crystal leg increases with an increase in temperature (Figure 7c).[23,24]

Leg Growth Rate. After the formation of the localized crystal deposit, the liquid is in contact with the substrate only at portions that eventually form the crystal legs. To formulate the average growth rate, we consider the evaporation of the liquid that forms thin liquid capillary bridges between the substrate and primary crystals (Figure 8a). The evaporation

near the liquid−solid interface is assumed to be diffusion-driven and depends on the substrate temperature. Assuming quasi-steady evaporation and the crystal legs to be cylindrical (Figure 8a), the concentration field around legs can be written as

$$\left(\frac{D}{r}\right) \frac{\partial}{\partial r} \left(\frac{r \partial C}{\partial r}\right) = 0 \tag{1}$$

where C is the concentration of water vapor at temperature T and D (m^2/s) is the diffusion coefficient of water vapor at temperature T. The evaporation flux ($j_r = -D(\partial C/\partial r)$) can be obtained from eq 1 using the boundary conditions: at $r = R_o$, $C = C_s(T_S)$ and at $r = R_\infty$, $C_\infty = \emptyset\, C_s(T_\infty)$; here, R_o is the radius of the leg, R_∞ is the distance where the vapor concentration reaches the far-field vapor concentration (C_∞), $\emptyset$ is the relative humidity, and $C_s(T_S)$ and $C_\infty(T_\infty)$ refer to the saturation vapor concentration (in kg/m^3) at T_s and T_∞. We obtain

$$j_r = -D \frac{\partial C}{\partial r} = -\frac{D}{r} \frac{(\emptyset C_\infty - C_s)}{\ln\left(\frac{r}{R_\infty}\right)} \tag{2}$$

Substituting $r = R_o$ in eq 2, we get

$$j_{R_o} = -\frac{D}{R_o} \frac{(\emptyset C_\infty - C_s)}{\ln\left(\frac{R_o}{R_\infty}\right)} \tag{3}$$

where j_{R_o} is the evaporation flux (kg/m^2 s) at the outer edge of the crystalline legs (R_o) and is dependent on R_∞. We take R_∞ = 500R_o since at $R_\infty \gg R_o$, j_{R_o} becomes independent of R_∞. The saturation concentration C_s and D are assumed to correspond to the substrate temperature.

After the formation of the secondary crystals, the saline solution wicks continuously into the crystal voids and forms a porous network due to high evaporation rates. We assume the porosity of the formed crystalline network as $\epsilon_p = 0.5$.[44,53] The movement of the liquid necessary to compensate for the evaporated liquid from the pores can be calculated from the evaporation flux taking into account the porosity of the crystal network as

$$j_{R_o} = \epsilon_p \rho_{sol}(dh_{sol}/dt) \quad (4)$$

where ρ_{sol} is the density of the saturated solution and dh_{sol}/dt denotes the wicking speed of the liquid into the crystal. The liquid that wicks into the pores forms secondary crystals as the solution is already in a saturated state. The rate of growth of the crystal height h_c at the interface of crystal legs can be written as

$$\rho_c \pi R_o^2 \frac{dh_c}{dt} = C_{sol}\rho_{sol}\pi R_o^2 \frac{dh_{sol}}{dt} \quad (5)$$

where C_{sol} is the w/w concentration of salt in water and ρ_c is the density of salt crystals at room temperature. Substituting for dh_{sol}/dt in eq 5, we get the crystal growth rate as

$$dh_c/dt = C_{sol}(\rho_{sol}/\rho_c)(j_{R_o}/\rho_{sol}\epsilon_p) \quad (6)$$

The evaporation flux (j_{R_o}) reduces with an increase in the leg radius (eq 3). We experimentally determine the leg radius (R_o) during the evaporation of a 3 μL droplet of saturated aqueous KCl on the PDMS substrate at different temperatures (inset of Figure 8c) (details in the Supplementary Information). The evaporation flux (eq 3) and the rate of growth of the crystal leg (eq 6) are calculated using the maximum and minimum radius of the crystal leg observed at different temperatures (shown as an inset in Figure 8c). The experimental values of the growth rate of the distinct crystal legs are calculated at different time instants of each experiment performed at different temperatures, and the average value is taken. The experimental growth rate is comparable with the calculated growth rate (Figure 8c). The formation of crystal legs on hydrophobic substrates suggests the possibility of removal of fouling caused by evaporative deposition by the use of the hydrophobic coating.

■ CONCLUSIONS

We report on the out-of-plane growth of crystal deposits during evaporation of saline droplets with high solubility on smooth and textured hydrophobic substrates with low contact line pinning. The liftoff behavior is shown to be independent of the type of salt, consistent across three different crystal habits, invariant to the chemistry of the hydrophobic coatings, and invariant to various initial droplet volumes at different substrate temperatures. The self-liftoff phenomenon is attributed to the formation of a network of primary crystals, which provides a pathway for preferential wetting and wicking of the saline liquid and results in dewetting of the underlying substrate. The evaporation of the capillary liquid bridge between the porous crystal network and the substrate leads to the formation and growth of secondary crystals that eventually

stack up to lift the crystal deposit from the substrate. Our model that takes into account the imbibition of the liquid into the porous crystal network and subsequent evaporation gives a good estimate for the growth rate of crystal legs with the substrate temperature.

■ ASSOCIATED CONTENT

ⓢ Supporting Information

The Supporting Information is available free of charge at https://pubs.acs.org/doi/10.1021/acs.langmuir.3c00214.

> Crystal habits of KCl, NaCl, KNO$_3$, and NH$_4$Cl; CA and contact diameter before nucleation during the evaporation of a droplet of the saturated saline solution of different salts on the R0PDMS substrate; horizontal growth during evaporative crystallization of aqueous sodium chloride; evaporation of a saline droplet of saturated aqueous calcium sulfate and aqueous KCl at a low concentration (0.00625C_{sat}) on the R0PDMS substrate; evaporation of a droplet of saturated aqueous KCl on different substrates at T = 80 °C; evaporation flux of a droplet on a heated hydrophobic surface; evaporation of a droplet of saturated aqueous KCl on R10Silane and R100Silane substrates at T = 80 °C; evaporation of a droplet of saturated aqueous KCl (V_i = 3 μL) on different hydrophobic substrates at room temperature; crystal leg diameter—experimental values; growth rate of crystal leg during evaporation in a droplet of aqueous saturated KCl on different substrates at T = 80 °C; and nucleation time and detachment time of the aqueous KCl droplet at different concentrations on the R0PDMS substrate (PDF)

> Supplementary Video S1: evaporation of a droplet of the saturated aqueous solution of KCl, NaCl, KNO$_3$, and NH$_4$Cl salts on the R0PDMS substrate at T = 80 °C (MP4)

> Supplementary Video S2: nucleation of crystals observed in a droplet of saturated aqueous KCl showing crystal nucleation near the triple contact line and on the liquid–air interface on the R0PDMS substrate at T = 50 and T = 70 °C (MP4)

> Supplementary Video S3: simultaneous side and bottom visualization of a droplet of saturated aqueous KCl with an initial volume = 3 μL evaporating on the R0PDMS substrate at T = 70 °C (MP4)

> Supplementary Video S4: evaporation of a droplet of saturated aqueous KCl on R10Silane and R100Silane substrates at T = 80 °C (MP4)

■ AUTHOR INFORMATION

Corresponding Author

Susmita Dash − *Department of Mechanical Engineering, Indian Institute of Science, Bengaluru 560012, India;* ⊙ orcid.org/0000-0003-0952-4209; Email: susmitadash@iisc.ac.in

Authors

Pranjal Agrawal − *Interdisciplinary Center for Energy Research, Indian Institute of Science, Bengaluru 560012, India*

Virkeshwar Kumar − *Department of Mechanical Engineering, Indian Institute of Technology, Kanpur 208016, India;* ⊙ orcid.org/0000-0001-6324-5679

Samantha McBride − *Department of Mechanical and Aerospace Engineering, Princeton University, Princeton, New Jersey 08544, United States;* ◉ orcid.org/0000-0002-6402-1359

Complete contact information is available at:
https://pubs.acs.org/10.1021/acs.langmuir.3c00214

Notes
The authors declare no competing financial interest.

■ REFERENCES

(1) Pan, S.-Y.; Snyder, S. W.; Packman, A. I.; Lin, Y. J.; Chiang, P.-C. Cooling Water Use in Thermoelectric Power Generation and Its Associated Challenges for Addressing Water-Energy Nexus. *Water-Energy Nexus* **2018**, *1*, 26−41.

(2) Averyt, K.; Macknick, J.; Rogers, J.; Madden, N.; Fisher, J.; Meldrum, J.; Newmark, R. Water Use for Electricity in the United States: An Analysis of Reported and Calculated Water Use Information for 2008. *Environ. Res. Lett.* **2013**, *8*, No. 015001.

(3) Feeley, T. J.; Skone, T. J.; Stiegel, G. J.; McNemar, A.; Nemeth, M.; Schimmoller, B.; Murphy, J. T.; Manfredo, L. Water: A Critical Resource in the Thermoelectric Power Industry. *Energy* **2008**, *33*, 1−11.

(4) Dash, S.; Rapoport, L.; Varanasi, K. K. Crystallization-Induced Fouling during Boiling: Formation Mechanisms to Mitigation Approaches. *Langmuir* **2018**, *34*, 782−788.

(5) Daer, S.; Kharraz, J.; Giwa, A.; Hasan, S. W. Recent Applications of Nanomaterials in Water Desalination: A Critical Review and Future Opportunities. *Desalination* **2015**, *367*, 37−48.

(6) Warsinger, D. M.; Swaminathan, J.; Guillen-Burrieza, E.; Arafat, H. A.; Lienhard, J. H., V Scaling and Fouling in Membrane Distillation for Desalination Applications: A Review. *Desalination* **2015**, *356*, 294−313.

(7) Song, S.; Demirel, Y. K.; De Marco Muscat-Fenech, C.; Tezdogan, T.; Atlar, M. Fouling Effect on the Resistance of Different Ship Types. *Ocean Eng.* **2020**, *216*, No. 107736.

(8) Boerlage, S. F. *Scaling and Particulate Fouling in Membrane Filtration Systems*; CRC Press, 2001; vol *26*.

(9) Kazi, S. N.; Teng, K. H.; Zakaria, M. S.; Sadeghinezhad, E.; Bakar, M. A. Study of Mineral Fouling Mitigation on Heat Exchanger Surface. *Desalination* **2015**, *367*, 248−254.

(10) Charles, N. T.; Johnson, D. W. The Occurrence and Characterization of Fouling during Membrane Evaporative Cooling. *J. Membr. Sci.* **2008**, *319*, 44−53.

(11) Garrett-Price, B. A.; Smith, S. A.; Watts, R. L.; Knudsen, J. G.; Marner, W. J.; Suitor, J. W. Fouling of Heat Exchangers. In *Characteristics, Costs, Prevention, Control, and Removal*; Noyes Publications: Norwich, NY, 1985; vol *599*, pp 19−21.

(12) Anderson, D. B. Relative Humidity or Vapor Pressure Deficit. *Ecology* **1936**, *17*, 277−282.

(13) Fukatani, Y.; Orejon, D.; Kita, Y.; Takata, Y.; Kim, J.; Sefiane, K. Effect of Ambient Temperature and Relative Humidity on Interfacial Temperature during Early Stages of Drop Evaporation. *Phys. Rev. E* **2016**, *93*, No. 043103.

(14) Shahidzadeh-Bonn, N.; Rafai, S.; Bonn, D.; Wegdam, G. Salt Crystallization during Evaporation: Impact of Interfacial Properties. *Langmuir* **2008**, *24*, 8599−8605.

(15) Diao, Y.; Myerson, A. S.; Hatton, T. A.; Trout, B. L. Surface Design for Controlled Crystallization: The Role of Surface Chemistry and Nanoscale Pores in Heterogeneous Nucleation. *Langmuir* **2011**, *27*, 5324−5334.

(16) Jenkins, A.; Wells, G. G.; Ledesma-Aguilar, R.; Orejon, D.; Armstrong, S.; McHale, G. Suppression of Crystallization in Saline Drop Evaporation on Pinning-Free Surfaces. *J. Chem. Phys.* **2023**, *158*, No. 124708.

(17) Deka, N.; Saha, S.; Dash, S. Evaporation-Induced Convective Transport in Confined Saline Droplets. *Colloids Surf., A* **2022**, *639*, No. 128256.

(18) Tarafdar, S.; Tarasevich, Y. Y.; Dutta Choudhury, M.; Dutta, T.; Zang, D. Droplet Drying Patterns on Solid Substrates: From Hydrophilic to Superhydrophobic Contact to Levitating Drops. *Adv. Condens. Matter Phys.* **2018**, *2018*, No. 5214924.

(19) Deegan, R. D.; Bakajin, O.; Dupont, T. F.; Huber, G.; Nagel, S. R.; Witten, T. A. Capillary Flow as the Cause of Ring Stains from Dried Liquid Drops. *Nature* **1997**, *389*, 827−829.

(20) McBride, S. A.; Dash, S.; Varanasi, K. K. Evaporative Crystallization in Drops on Superhydrophobic and Liquid-Impregnated Surfaces. *Langmuir* **2018**, *34*, 12350−12358.

(21) Kumar, V.; Dash, S. Patterns during Evaporative Crystallization of a Saline Droplet. *Langmuir* **2022**, *38*, 10265−10273.

(22) Shin, B.; Moon, M. W.; Kim, H. Y. Rings, Igloos, and Pebbles of Salt Formed by Drying Saline Drops. *Langmuir* **2014**, *30*, 12837−12842.

(23) Salim, H.; Kolpakov, P.; Bonn, D.; Shahidzadeh, N. Self-Lifting NaCl Crystals. *J. Phys. Chem. Lett.* **2020**, *11*, 7388−7393.

(24) McBride, S. A.; Girard, H. L.; Varanasi, K. K. Crystal Critters: Self-Ejection of Crystals from Heated Superhydrophobic Surfaces. *Sci. Adv.* **2021**, *7*, 1−9.

(25) Wang, F.; Tian, S.; Yuan, Q. Evaporation-Induced Crystal Self-Assembly (EICSA) of Salt Drops Regulated by Trace of Polyacrylamide. *Colloids Surf., A* **2022**, *644*, No. 128856.

(26) Mullin, J. W. *Crystallization*; Elsevier, 2001.

(27) Zettsu, N.; Kida, S.; Uchida, S.; Teshima, K. Sub-2 Nm Thick Fluoroalkylsilane Self-Assembled Monolayer-Coated High Voltage Spinel Crystals as Promising Cathode Materials for Lithium Ion Batteries. *Sci. Rep.* **2016**, *6*, 31999.

(28) Hu, H.; Larson, R. G. Evaporation of a Sessile Droplet on a Substrate. *J. Phys. Chem. B* **2002**, *106*, 1334−1344.

(29) Erbil, H. Y.; McHale, G.; Newton, M. I. Drop Evaporation on Solid Surfaces: Constant Contact Angle Mode. *Langmuir* **2002**, *18*, 2636−2641.

(30) Basu, N.; Mukherjee, R. Evaporative Drying of Sodium Chloride Solution Droplet on a Thermally Controlled Substrate. *J. Phys. Chem. B* **2020**, *124*, 1266−1274.

(31) Rasheed, A.; Sharma, S.; Kabi, P.; Saha, A.; Chaudhuri, S.; Basu, S. Precipitation Dynamics of Surrogate Respiratory Sessile Droplets Leading to Possible Fomites. *J. Colloid Interface Sci.* **2021**, *600*, 1−13.

(32) De Yoreo, J. J.; Vekilov, P. G. Principles of crystal nucleation and growth. *Rev. Mineral. Geochem.* **2003**, *54*, 57−93.

(33) Washburn, E. R. The Creeping of Solutions. *J. Phys. Chem.* **1927**, *31*, 1246−1248.

(34) Hazlehurst, T. H.; Martin, H. C.; Brewer, L. The Creeping of Saturated Salt Solutions. *J. Phys. Chem.* **1936**, *40*, 439−452.

(35) Kuznetsov, G. V.; Misyura, S. Y.; Volkov, R. S.; Morozov, V. S. Marangoni Flow and Free Convection during Crystallization of a Salt Solution Droplet. *Colloids Surf., A* **2019**, *572*, 37−46.

(36) Misyura, S. Y. Different Modes of Heat Transfer and Crystallization in a Drop of NaCl Solution: The Influence of Key Factors on the Crystallization Rate and the Heat Transfer Coefficient. *Int. J. Therm. Sci.* **2021**, *159*, No. 106602.

(37) Veran-Tissoires, S.; Marcoux, M.; Prat, M. Discrete salt crystallization at the surface of a porous medium. *Phys. Rev. Lett.* **2012**, *108*, No. 054502.

(38) Licsandru, G.; Prat, M. Enhanced Transport in a Porous Medium Due to Dissolved Salt. *Phys. Rev. Fluids* **2022**, *7*, No. 064304.

(39) Bigioni, T. P.; Lin, X.-M.; Nguyen, T. T.; Corwin, E. I.; Witten, T. A.; Jaeger, H. M. Kinetically Driven Self Assembly of Highly Ordered Nanoparticle Monolayers. *Nat. Mater.* **2006**, *5*, 265−270.

(40) Azimi, G.; Cui, Y.; Sabanska, A.; Varanasi, K. K. Scale-Resistant Surfaces: Fundamental Studies of the Effect of Surface Energy on Reducing Scale Formation. *Appl. Surf. Sci.* **2014**, *313*, 591−599.

(41) Sojoudi, H.; Nemani, S. K.; Mullin, K. M.; Wilson, M. G.; Aladwani, H.; Lababidi, H.; Gleason, K. K. Micro-/Nanoscale Approach for Studying Scale Formation and Developing Scale-Resistant Surfaces. *ACS Appl. Mater. Interfaces* **2019**, *11*, 7330−7337.

(42) Chen, H.; Tang, T.; Amirfazli, A. Liquid Transfer Mechanism between Two Surfaces and the Role of Contact Angles. *Soft Matter* **2014**, *10*, 2503−2507.

(43) Chen, H.; Tang, T.; Zhao, H.; Law, K. Y.; Amirfazli, A. How Pinning and Contact Angle Hysteresis Govern Quasi-Static Liquid Drop Transfer. *Soft Matter* **2016**, *12*, 1998−2008.

(44) Dai, S.; Shin, H.; Santamarina, J. C. Formation and Development of Salt Crusts on Soil Surfaces. *Acta Geotech.* **2016**, *11*, 1103−1109.

(45) Misyura, S. The Dependence of Evaporation and Crystallization Kinetics on Dynamic and Thermal Background. *AIChE J.* **2020**, *66*, No. e16282.

(46) Zhang, H.; Weber, S. G. Teflon AF Materials. *Top. Curr. Chem.* **2011**, 307−337.

(47) Popov, Y. O. Evaporative Deposition Patterns: Spatial Dimensions of the Deposit. *Phys. Rev. E: Stat., Nonlinear, Soft Matter Phys.* **2005**, *71*, No. 036313.

(48) Sobac, B.; Brutin, D. Thermal Effects of the Substrate on Water Droplet Evaporation. *Phys. Rev. E: Stat., Nonlinear, Soft Matter Phys.* **2012**, *86*, No. 021602.

(49) Papadopoulos, P.; Mammen, L.; Deng, X.; Vollmer, D.; Butt, H. J. How Superhydrophobicity Breaks Down. *Proc. Natl. Acad. Sci. U. S. A.* **2013**, *110*, 3254−3258.

(50) Lafuma, A.; Quéré, D. Superhydrophobic States. *Nat. Mater.* **2003**, *2*, 457−460.

(51) Paxson, A. T.; Varanasi, K. K. Self-Similarity of Contact Line Depinning from Textured Surfaces. *Nat. Commun.* **2013**, *4*, 1492.

(52) Sharma, S.; Jain, S.; Saha, A.; Basu, S. Evaporation Dynamics of a Surrogate Respiratory Droplet in a Vortical Environment. *J. Colloid Interface Sci.* **2022**, *623*, 541−551.

(53) Roy, R.; Weibel, J. A.; Garimella, S. V. Modeling the Formation of Efflorescence and Subflorescence Caused by Salt Solution Evaporation from Porous Media. *Int. J. Heat Mass Transfer* **2022**, *189*, No. 122645.